



**HAL**  
open science

# A Spectra Classification Methodology of Hyperspectral Infrared Images for Near Real-Time Estimation of the SO<sub>2</sub> Emission Flux from Mount Etna with LARA Radiative Transfer Retrieval Model

Charlotte Segonne, Nathalie Huret, Sébastien Payan, Mathieu Gouhier,  
Valéry Catoire

## ► To cite this version:

Charlotte Segonne, Nathalie Huret, Sébastien Payan, Mathieu Gouhier, Valéry Catoire. A Spectra Classification Methodology of Hyperspectral Infrared Images for Near Real-Time Estimation of the SO<sub>2</sub> Emission Flux from Mount Etna with LARA Radiative Transfer Retrieval Model. *Remote Sensing*, 2020, EO for Mapping Natural Resources and Geohazards, 12 (24), pp.4107. 10.3390/rs12244107 . hal-03101521

**HAL Id: hal-03101521**

**<https://uca.hal.science/hal-03101521v1>**

Submitted on 7 Jan 2021

**HAL** is a multi-disciplinary open access archive for the deposit and dissemination of scientific research documents, whether they are published or not. The documents may come from teaching and research institutions in France or abroad, or from public or private research centers.

L'archive ouverte pluridisciplinaire **HAL**, est destinée au dépôt et à la diffusion de documents scientifiques de niveau recherche, publiés ou non, émanant des établissements d'enseignement et de recherche français ou étrangers, des laboratoires publics ou privés.



Distributed under a Creative Commons Attribution 4.0 International License

Article

# A Spectra Classification Methodology of Hyperspectral Infrared Images for Near Real-Time Estimation of the SO<sub>2</sub> Emission Flux from Mount Etna with LARA Radiative Transfer Retrieval Model

Charlotte Segonne <sup>1,\*</sup> , Nathalie Huret <sup>1</sup> , Sébastien Payan <sup>2</sup>, Mathieu Gouhier <sup>3</sup> and Valéry Catoire <sup>4</sup>

<sup>1</sup> Laboratoire Météorologie Physique, Centre National de la Recherche Scientifique, Université Clermont Auvergne, Observatoire de Physique du Globe de Clermont-Ferrand, F-63000 Clermont-Ferrand, France; n.huret@opgc.fr

<sup>2</sup> Laboratoire Atmosphères Milieux Observations Spatiales, Centre National de la Recherche Scientifique, Sorbonne Université, Université de Versailles-Saint-Quentin-en-Yvelines, F-75252 Paris, France; sebastien.payan@sorbonne-universite.fr

<sup>3</sup> Laboratoire Magmas Volcans, Centre National de la Recherche Scientifique, Université Clermont Auvergne, Observatoire de Physique du Globe de Clermont-Ferrand, F-63000 Clermont-Ferrand, France; M.Gouhier@opgc.univ-bpclermont.fr

<sup>4</sup> Laboratoire de Physique et Chimie de l'Environnement et de l'Espace, Centre National de la Recherche Scientifique, Université Orléans, Centre National d'Etudes Spatiales, F-45071 Orléans CEDEX 2, France; valery.catoire@cnsr-orleans.fr

\* Correspondence: charlotte.segonne@uca.fr

Received: 10 November 2020; Accepted: 10 December 2020; Published: 16 December 2020



**Abstract:** Fast and accurate quantification of gas fluxes emitted by volcanoes is essential for the risk mitigation of explosive eruption, and for the fundamental understanding of shallow eruptive processes. Sulphur dioxide (SO<sub>2</sub>), in particular, is a reliable indicator to predict upcoming eruptions, and its systemic characterization allows the rapid assessment of sudden changes in eruptive dynamics. In this regard, infrared (IR) hyperspectral imaging is a promising new technology for accurately measure SO<sub>2</sub> fluxes day and night at a frame rate down to 1 image per second. The thermal infrared region is not very sensitive to particle scattering, which is an asset for the study of volcanic plume. A ground based infrared hyperspectral imager was deployed during the IMAGETNA campaign in 2015 and provided high spectral resolution images of the Mount Etna (Sicily, Italy) plume from the North East Crater (NEC), mainly. The LongWave InfraRed (LWIR) hyperspectral imager, hereafter name Hyper-Cam, ranges between 850–1300 cm<sup>-1</sup> (7.7–11.8 μm). The LATMOS (Laboratoire Atmosphères Milieux Observations Spatiales) Atmospheric Retrieval Algorithm (LARA), which is used to retrieve the slant column densities (SCD) of SO<sub>2</sub>, is a robust and a complete radiative transfer model, well adapted to the inversion of ground-based remote measurements. However, the calculation time to process the raw data and retrieve the infrared spectra, which is about seven days for the retrieval of one image of SO<sub>2</sub> SCD, remains too high to infer near real-time (NRT) SO<sub>2</sub> emission fluxes. A spectral image classification methodology based on two parameters extracting spectral features in the O<sub>3</sub> and SO<sub>2</sub> emission bands was developed to create a library. The relevance is evaluated in detail through tests. From data acquisition to the generation of SO<sub>2</sub> SCD images, this method requires only ~40 s per image, which opens the possibility to infer NRT estimation of SO<sub>2</sub> emission fluxes from IR hyperspectral imager measurements.

**Keywords:** volcanic plume; SO<sub>2</sub> emission flux; passive degassing; remote sensing; spectra image classification; hyperspectral; infrared

## 1. Introduction

More than 500 million people live within the potential exposure range of a volcano [1]. Monitoring volcanoes is then essential and involves different types of measurements, such as volcanic degassing, seismicity, and ground deformation detection [2]. Volatiles, in particular, are a crucial component of volcanic systems. The explosivity of an eruption depends, in large part, on the amount and composition of gas contained in the erupted magma. For that reason, measurements of volcanic degassing have been one of the most widely used methods in volcanic monitoring networks for more than 40 years. The shallow exsolution depth of SO<sub>2</sub>, compared to carbon dioxide (CO<sub>2</sub>), makes it a good indicator of the presence of a magmatic body near the surface, and, therefore, provides a tool to forecast eruptions. Fluctuations in degassing levels may reflect changes in the magma supply rate and help inform a short-term forecast of on-going eruptions [3–8]. Moreover, the composition of volcanic gases offers insight into physical processes occurring at depth [9,10]. In addition to the risks induced by volcanic eruptions, monitoring the volcanoes degassing emissions in the atmosphere is important for an environmental impact and a hazardous effect on human health. After H<sub>2</sub>O and CO<sub>2</sub>, sulfur dioxide is the main volcanic gas emitted by volcanoes. It is widely monitored due to its low background atmospheric abundance. The impact of SO<sub>2</sub> emission on atmospheric chemistry and the estimation of the global budget of SO<sub>2</sub> in the atmosphere induced by volcanoes are part of climate and environmental monitoring as well as public health prevention [11]. The oxidation of SO<sub>2</sub> leads to the formation of sulfur aerosols responsible for acid rain [12], problems on vegetation growth close to volcanoes, and cause asthma or respiratory problems to humans [13,14].

Mount Etna mean SO<sub>2</sub> flux is equivalent, for example, to the total anthropogenic SO<sub>2</sub> emissions from France [12]. It is the largest active volcano in Europe and the world's strongest permanent contributor of volcanic volatiles to the atmosphere [15], which makes it one of the most monitored volcanoes of the planet [2]. The accurate characterization of its gas emission fluxes is, hence, the purpose of many studies.

Volcanic gas emissions are mostly monitored by satellites as well as by ground-based instruments. The satellite-based instruments remotely measuring SO<sub>2</sub> use different channels and absorption bands such as OMI (Ozone Monitoring Instrument) [16,17] and TROPOMI (Tropospheric Monitoring Instrument) [18,19] in the ultraviolet (UV), MODIS (Moderate-Resolution Imaging Spectroradiometer), SEVIRI (Spinning Enhanced Visible and Infrared Imager) [20,21], IASI (Infrared Atmospheric Sounding Interferometer), and AIRS (Atmospheric InfraRed Sounder) [22,23] in the infrared (IR). Ground-based monitoring is performed remotely using ultraviolet (UV) cameras [24], mini-DOAS (Differential Optical Absorption Spectroscopy) instruments [25,26], and IR cameras [27]. The NOVAC (Network for Observation of Volcanic and Atmospheric Change) project with the deployment of fully automated mini-DOAS systems used in a scanning mode has permit to get the first real-time determinations of SO<sub>2</sub> flux in a monitoring system [28]. This system allows the monitoring of nearly 20 volcanoes around the world [29]. In 2004, the FLAME (FLux Automatic MEasurements) network was developed and installed by the Istituto Nazionale Geofisica e Vulcanologia (INGV) (Catania, Sicily) on Mount Etna flanks with nine UV scanning spectrometers to automatically get SO<sub>2</sub> fluxes in real-time and with a high frequency [30]. The network collects data daily during the daytime with a complete scan every ~5 min [31]. The SO<sub>2</sub> flux emissions of the different vents of Mount Etna from the FLAME network reveals shifts in the activity of each vent approaching an eruptive episode [5,32].

Ground-based hyperspectral infrared imaging systems of volcanic degassing offer high spatial, spectral, and temporal resolution measurements [33,34]. Such imagers can provide continuous day and night measurements, which is likely the most important advantage over UV imagers, but also essential to monitor volcanoes located in high latitude regions during the wintertime. Commercial hyperspectral IR imagers are still an expensive technology, which may be more attractive in the near future with the increase of possible applications and the development of studies and algorithms aiming at exploiting all the capacities of such instruments. Nevertheless, some recent advances on the development of uncooled detector technology allow the use of cheap thermal infrared imagers to

quantify hazardous gases. Wright et al. (2013) presented the characteristics of a thermal hyperspectral imager with ~30 spectral bands in the 8–14  $\mu\text{m}$  wavelength region [35].

Hyperspectral imaging is an interesting and powerful tool in a wide range of applications such as agriculture, forestry, and environmental management [36], geological exploitation and mineralogy, urban planning, and disaster prediction, military and defense [37], but also remote sensing of volcanic plume for gas emissions monitoring. The vast amount of data comprised in the spectra of the images obtained with this kind of instrument makes it heavy to process and induce to set up a methodology for classifying the pixels of an image to get the most information of the spectral signature in near real-time. Different deep-learning methods exist, including supervised or unsupervised, parametric or non-parametric ones. Paoletti et al. (2019) reviewed the different popular models and architectures used for the classification of remotely sensed hyperspectral spectral images [38]. To achieve a successful classification of the image pixels, many factors and steps are involved, starting with the determination of a suitable classification system, selection of training samples, image preprocessing, feature extraction, selection of suitable classification approaches, post-classification processing, and accuracy assessment [39].

When pixels of images are spectra like in this study, the goal of image pixels classification is to identify different patterns in spectra with an automated methodology in order to extract information from data and create a set of reference spectra. Many classification approaches have been developed depending on the domain of application. For example, Van Damme et al. (2017) present a version of a neural-network-based algorithm developed to retrieve in near real-time the ammonia columns from the satellite observations from the hyperspectral imager IASI [40].

A methodology to analyze the large amount of data produced by such technology is necessary to respond to the need of NRT knowledge of volcanic gas emission fluxes.

In this paper, we present a spectral image classification methodology for infrared hyperspectral images from Mount Etna volcanic plume. The objective is to achieve a fast and accurate retrieval of volcanic plume in order to get the  $\text{SO}_2$  emission flux in NRT, which is essential for early warning and mitigation of volcanic risk.

In the next section, we describe the dataset from the IMAGETNA field campaign and the LARA model (LATMOS (Laboratoire Atmosphères Milieux Observations Spatiales) Atmospheric Retrieval Algorithm) used to retrieve the data, and we present the method. More detailed information about the IMAGETNA and LARA model are presented in Huret et al. 2019 [34]. Then, we bring step-by-step the pixels classification methodology that we applied to our dataset. The results of the classification and the flux estimations are presented in Section 3 and discussed in Section 4. The last section is dedicated to the conclusions and perspective of this study.

## 2. Materials and Methods

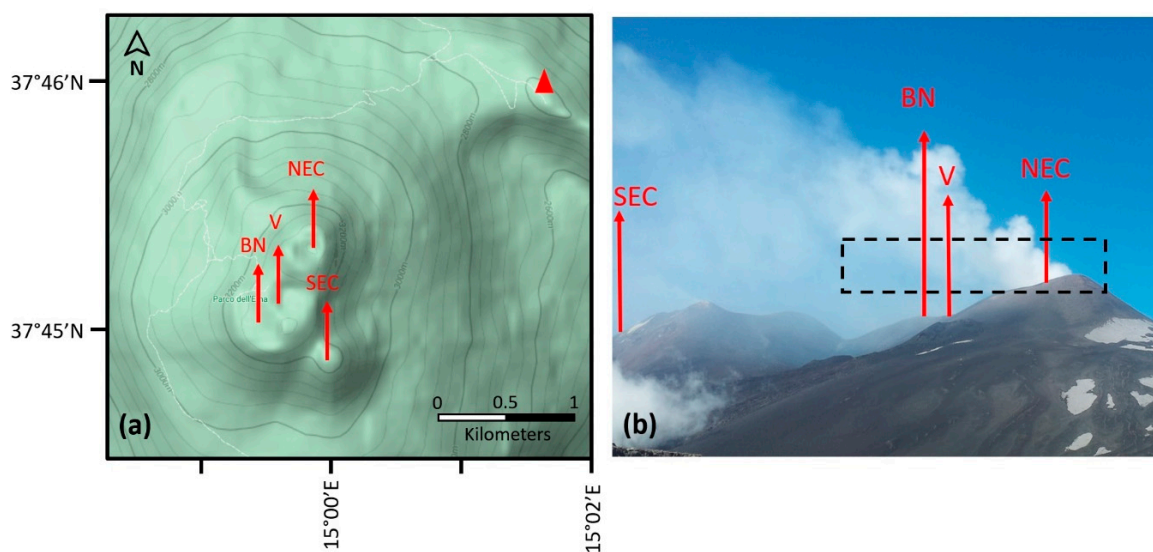
### 2.1. Overview of the Data

The IMAGETNA campaign was held from 21–26 June 2015 from the Pizzi De Neri Volcano observatory on the North side of Mount Etna at 2850 m altitude and at ~2 km from the plume. One of the purposes of the field campaign was to make remote observations of the plume of Mount Etna using the infrared imager Hyper-Cam developed by Telops company, during a quiescent stage of its activity. The first days of the campaign were dedicated to instrumentation deployment and basic tests. The weather during the campaign was very good, with mainly cloudless skies, allowing us to carry out a large number of measurements in good conditions.

The Hyper-Cam is a passive infrared hyperspectral imaging system with a spectral range of 840–1300  $\text{cm}^{-1}$  (7.7–11  $\mu\text{m}$ ). This camera combines a high spatial resolution with images containing up to 320  $\times$  256 pixels, a maximum field of view of 6.4°  $\times$  5.1°, and spectral resolutions from 0.25 to 150  $\text{cm}^{-1}$ . Considering the geographical arrangement of the campaign and the parameterization of the hyperspectral imager in relation to the Etna plume, the surface of each pixel is 7.84  $\text{m}^2$

(i.e.,  $2.8 \times 2.8$  m). The Hyper-Cam is radiometrically calibrated using two blackbodies with different temperatures with a spectral radiometric accuracy of 0.5 K at a blackbody temperature of 30 °C [41]. Each measured image has three dimensions: two spatial dimensions and one spectral dimension.




As shown in Figure 1a, Mount Etna has several active craters pointed out with red arrows: the two central craters (Bocca Nuova (BN) and Voragine (V)), the North East crater (NEC), and the South East craters (SEC), which is the one created most recently [42]. To get the maximum thermal contrast between the plume and the background, the measurements were done early in the morning starting at around 8:00 UTC. Considering the direction of the plume propagation and the location of the observatory where the measurements have been done, the plume captured by the Hyper-Cam imager during the field campaign is mainly related to the North East Crater (NEC) of Mount Etna. An example of projection of the contours of the acquired images is superimposed on Figure 1b. This projected image corresponds to an image of  $[320 \times 64]$  pixels.



**Figure 1.** (a) Map of Mount Etna area (© Google Maps) showing the location of the four different craters with red arrows: Bocca Nuova (BN), Voragine (V), North East crater (NEC), South East crater (SEC), and the location of the Pizzi De Neri observatory with a red triangle. (b) Picture taken from the measurement platform of the Pizzi De Neri observatory during the IMAGETNA campaign with an example of the Hyper-Cam projected image, represented by a black dashed rectangle, and the hand estimated location of the four craters (SEC, NEC, BN, and V) pointed out with red arrows.

A trade-off is necessary between the high spectral and spatial resolutions and the temporal resolution to capture the dynamism of the measured scene. Table 1 presents the main characteristics of the three sequences reported in this study such as spectral resolution, from 2 to 4  $\text{cm}^{-1}$ , and the acquisition time, from  $\sim 1.3$  to  $\sim 4.6$  s, resulting from the trade-off made for each sequence. All the images have 20,480 pixels (i.e.,  $320 \times 64$  pixels). The field of view includes part of the ground, the plume, and the clear sky. The dataset is composed of  $\sim 900$  images representing over 18 million of pixels and  $\sim 35$  min of measurements.

**Table 1.** Characteristics of the selected measurement sequences from the IMAGETNA Campaign.

#	Date Time	Spectral Resolution (cm <sup>-1</sup> )	Image Acquisition Time	Number of Images	Total Number of Pixels	Sequence Duration	Broadband IR Image
A	23-06-2015 08:12:45 – 08:22:22 (UTC *)	2	4.595 s	120	$2.46 \times 10^{-6}$	9'37"	
B	26-06-2015 08:25:25 – 08:38:50 (UTC)	2	2.547 s	288	$5.90 \times 10^{-6}$	13'25"	
C	26-06-2015 07:17:59 – 07:29:02 (UTC)	4	1.274 s	470	$9.63 \times 10^{-6}$	11'03"	

\* UTC: Universal Time Coordinated.

The three sequences, to investigate SO<sub>2</sub> emissions fluxes, have been selected among the other sequences because of their cloud-free conditions but also because they have a common measurement geometry with an unchanged location and distance of the camera with respect to the plume. Moreover, the meteorological conditions are close in term of temperature and wind direction, which is roughly horizontal southeasterly. With such similarities, we can extract information from the data by developing data processing to the three cases. The acquisition times are of the order of a few seconds, allowing us to finely capture the dynamics of the plume and, hence, the SO<sub>2</sub> emission flux.

## 2.2. Retrieval Model: LARA

The data retrieval of SO<sub>2</sub> slant column densities has been performed with the LATMOS Atmospheric Retrieval Algorithm (LARA). LARA is a radiative transfer model associated with a minimization algorithm of the Levenberg-Marquardt type [43], which has been developed and adapted, in the last decade [44,45], to both nadir and limb geometries, and to balloon, satellite, or ground-based experiments [46–48]. It takes into account the geometry of the plume, the thickness and the altitude, and different chemical species, H<sub>2</sub>O, CO<sub>2</sub>, O<sub>3</sub>, CH<sub>4</sub>, NO<sub>2</sub>, and SO<sub>2</sub>. The radiative transfer is calculated in each pixel with a profile along the line of sight divided in more than 40 layers from the instrument altitude of 2.85 km up to the top of the atmosphere at 100 km. The model also considers the contribution of particles in the IR spectra as well as the water vapor continuum [49]. Huret et al. 2019 [34] present the different tests to configure the model and results of the SO<sub>2</sub> slant column densities (SCD) retrievals. The sensitivity of the retrieval to the parameters of the geometry of the plume, such as the plume altitude, its thickness, and the additional temperature with respect to ambient temperature, highlighted a low influence of those parameters on the SO<sub>2</sub> SCD in the dilute part of the plume. That study demonstrated that LARA is a robust and well adapted model to ground-based remote sensing of volcanic plume measurements.

The main downside of LARA is the calculation time to retrieve each image pixel-by-pixel. For example, the retrieval of an image of [320 × 64] pixels with 60 spectral points in the SO<sub>2</sub> spectral band requires one week of calculation on the computers of AERIS data center ([www.aeris-data.fr](http://www.aeris-data.fr)) to be able to image the SO<sub>2</sub> slant column densities. This method is very expensive in term of calculation time and cannot be applied to process all other sequences from the IMAGETNA campaign. To make the most of the capabilities of this kind of IR hyperspectral imager and to reach quasi real-time estimation of the SO<sub>2</sub> flux, developing a methodology to significantly reduce the calculation time of SO<sub>2</sub> SCD retrieval is crucial.

Five images of one of the sequences measured on 26 June 2015 have been previously processed pixel-by-pixel using the LARA model for the study presented in Huret et al. 2019 [34]. Already retrieved images of SO<sub>2</sub> SCD (ppm m) can easily be converted into mass of SO<sub>2</sub> per surface unit (g m<sup>-2</sup>) using Equation (1).

$$SO_2 \text{ (g.m}^{-2}\text{)} = \frac{SO_2 \text{ (ppm.m)} \times M_{SO_2}}{V_{M_{air}}} \times 10^{-3} \quad (1)$$

with the molar mass of SO<sub>2</sub>  $M_{SO_2} = 64.06 \text{ g mol}^{-1}$  and the molar volume of air  $V_{M_{air}} = 33.2 \text{ L mol}^{-1}$  with a pressure of 692 hPa and a temperature of 276 K at Mount Etna altitude of 3300 m from Trapani meteorological sounding data performed on the days of the campaign. Figure 2 presents an example of the SO<sub>2</sub> mass per surface unit obtained in g m<sup>-2</sup> in the range of 0.02 to 30 g m<sup>-2</sup> for the image of 26 June 2015 at 08:25:44 UTC. As previously mentioned in Section 2.1, each pixel has a surface of 7.84 m<sup>2</sup>. Hence, the image used as an example contains a total mass of SO<sub>2</sub> of ~560 kg.

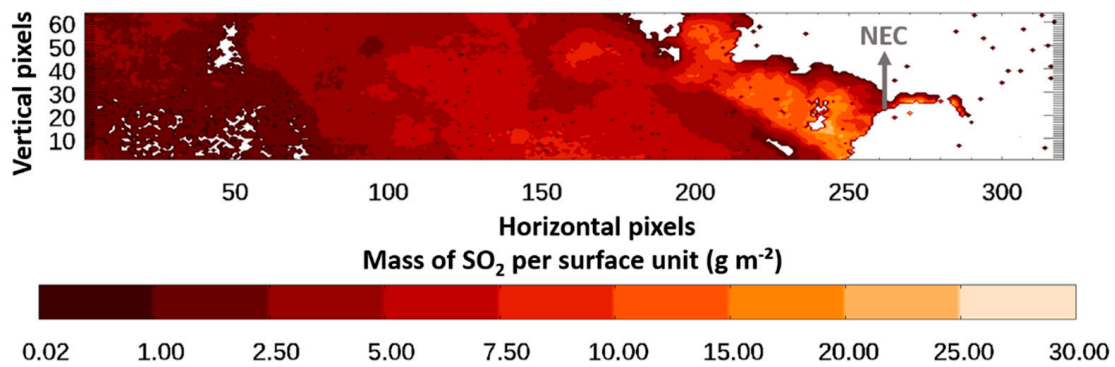


**Figure 2.** Example of the mass of SO<sub>2</sub> per surface unit in g m<sup>-2</sup> for 26 June 2015—08:25:44 UTC image retrieved pixel-by-pixel with the LARA model. The grey arrow indicates the NEC location.

### 2.3. Massive Retrieval Methodology

The objective here is to define the architecture of a network, based on characteristic features in the brightness temperature (BT) spectra, from which information leading to fast and accurate determination of the SO<sub>2</sub> SCD in each pixel can be extracted.

#### 2.3.1. Hyper-Cam Spectral Band Analysis

The spectral range of the Hyper-Cam encompasses in particular the O<sub>3</sub> and the SO<sub>2</sub> emission bands at (1000–1100) cm<sup>-1</sup> and (1100–1200) cm<sup>-1</sup>, respectively, as shown in Figure 3a. The emission line intensities of O<sub>3</sub>, SO<sub>2</sub>, and H<sub>2</sub>O extracted from the GEISA (Gestion et Etude des Informations Spectroscopiques Atmosphériques) spectroscopic database and simulated with a GEISA graphical tool (<https://geisa.aeris-data.fr/>), with an average spectral resolution greater than 0.2 cm<sup>-1</sup>, are presented in Figure 3a,b. Figure 3a shows well-defined spectral emission regions for O<sub>3</sub> and SO<sub>2</sub>, which are independent from each other and can, therefore, provide specific information from either spectral window. The signal due to O<sub>3</sub> emission lines can be considered as two continuous well identified branches. The SO<sub>2</sub> emission line intensities are less intense, with two flatted wings. H<sub>2</sub>O has several emission lines in the SO<sub>2</sub> spectral range [1100–1200] cm<sup>-1</sup> (see Figure 3b), which contribute to the signal. Since the water vapor column is retrieved simultaneously to SO<sub>2</sub>, H<sub>2</sub>O emission lines are then well fitted. Aerosols and droplets are parameterized and considered as a first-order modelling with a spectral dependency of the plume optical thickness (see Huret et al. 2019 for more details) [34]. Figure 3c presents different examples of BT spectra extracted from the images of the third sequence of 26 June 2015 (sequence B in Table 1). The presence of O<sub>3</sub>, SO<sub>2</sub>, and H<sub>2</sub>O is recognizable with more or less intensity in those example spectra depending on the part of the image they are related to. The spectral signatures in those images denote the ground in green, the sky without plume in red, the plume with different levels of dilution (in orange and blue), with more or less water vapor, droplets, and aerosols. The brightness temperature is the temperature a black body would have if it has the same radiance as the one measured by Hyper-Cam.



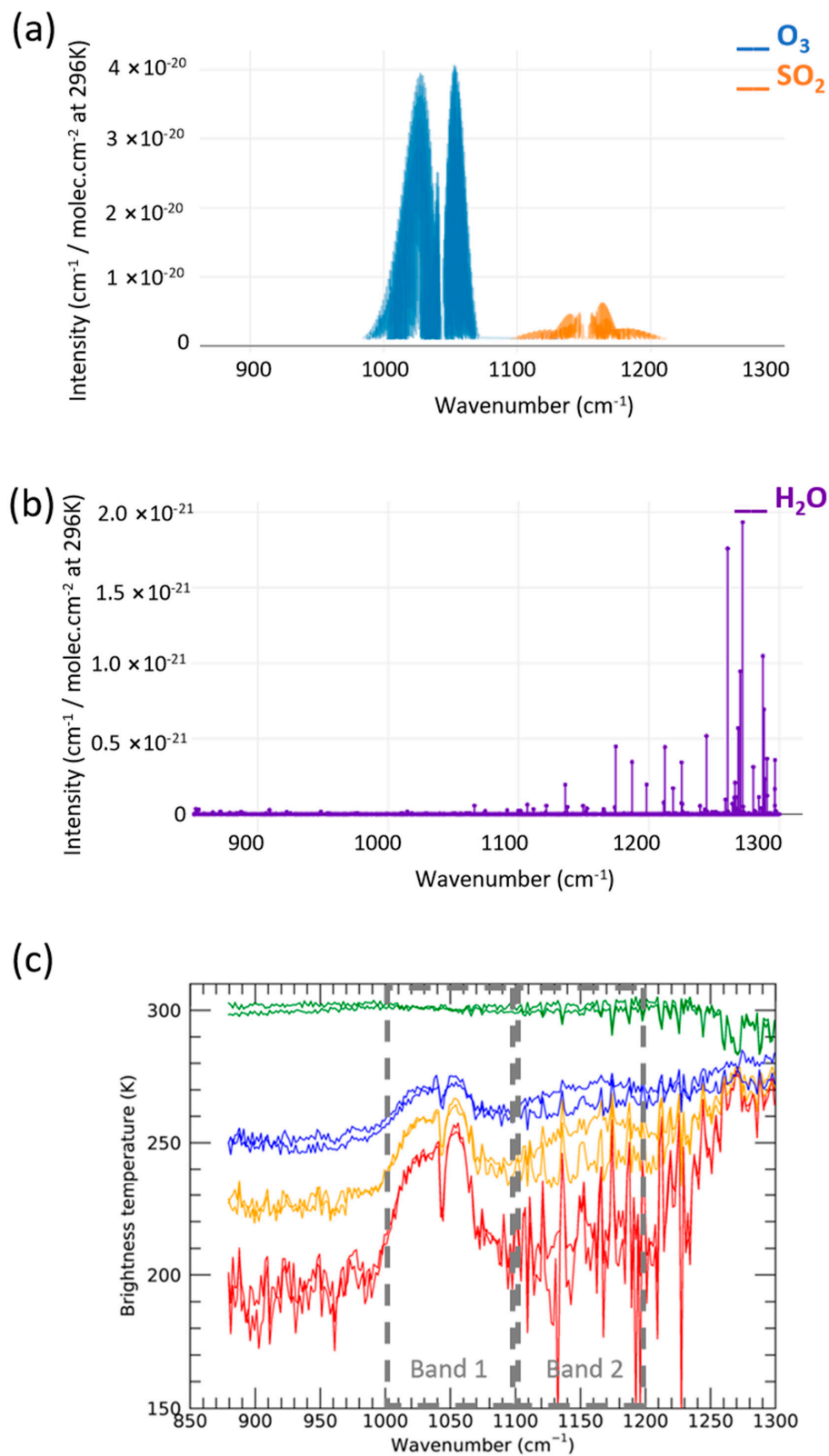


**Figure 3.** Emission line intensities of (a)  $\text{O}_3$  in blue,  $\text{SO}_2$  in orange, and (b) of  $\text{H}_2\text{O}$  in purple simulated with the GEISA graphical tool between 850 and 1300  $\text{cm}^{-1}$ . (c) Examples of spectra from 26 June 2015 dataset with: ground spectra in green, dense plume spectra in blue, diluted plume spectra in orange, and clear sky spectra in red. The grey dashed boxes identify the spectral bands 1 and 2 chosen for the image classification.

### 2.3.2. O<sub>3</sub> Emission Region: Spectral “Band 1”

The first spectral band considered here is situated in the range of 1000–1100 cm<sup>-1</sup> characteristic of O<sub>3</sub>. Different examples of BT spectra from the measurements on 26 June 2015 with a spectral resolution of 2 cm<sup>-1</sup> are given on Figure 3c. We can easily identify the ozone emission region, defined as Band 1, thanks to its typical rovibrational branches in the clear sky, the diluted plume, and the less diluted plume pixels, corresponding respectively to red, orange, and blue spectra. The ozone band in the clear sky is strong and characteristic of stratospheric ozone. The less diluted and opaque the plume is, the flatter the ozone branches are. As for the green spectra corresponding to ground pixels, the ozone is not relevant. Hence, the spectra are flat with an average BT value of 300 K. By calculating the integrated BT values in Band 1, we extract a spectral feature, identifying if we have a ground, a clear sky, or a plume pixel spectrum. The lowest values correspond to a clean atmosphere (i.e., plume free atmosphere), ~22,950 K cm<sup>-1</sup> for red spectra in Figure 3c, and the highest values to a very opaque plume or even ground pixel, ~26,450 and ~29,950 K cm<sup>-1</sup> for blue and green spectra in Figure 3c, respectively.

### 2.3.3. SO<sub>2</sub> Emission Region: Spectral “Band 2”

The second spectral band considered here is in the range of 1100–1200 cm<sup>-1</sup>, which is the SO<sub>2</sub> spectral band. Inside Band 2 in Figure 3c, we can see that the clear sky BT is the lowest with an average value of 200 K. A bump shape of the spectra in the diluted and less diluted pixels (orange and blue spectra, respectively) highlights the presence of SO<sub>2</sub> in the plume and the few more intense peaks are significant of the water vapor emission lines. The BT in the SO<sub>2</sub> spectral region increases along with the increase of SO<sub>2</sub> concentration inside the plume. By calculating the mean BT values in Band 2, we extract another spectral feature from the data, which is characteristic of the SO<sub>2</sub> concentration in the spectra. For the images of the IMAGETNA campaign previously presented in Table 1, the plume mean BT varies between 200 and 300 K in the clear sky and ground, respectively.

The architecture of the classification network is composed of two layers. The first layer categorizes the pixels with regard to their main characteristic, which is either a ground, plume, or clear sky pixel using Band 1. An index  $I_{O_3}$  corresponding to the integrated value of the BT in the O<sub>3</sub> spectral region is attributed to each spectrum. Then, the second layer gives information about the concentration in SO<sub>2</sub>. The second index,  $I_{SO_2}$ , attributed to each spectrum corresponds to the mean BT in the SO<sub>2</sub> spectral region. Each spectral feature is extracted and classified following the mapping function  $Y = f(I_{O_3}, I_{SO_2})$ , which assigns a vector label to each pixel.

## 2.4. SO<sub>2</sub> Emission Flux Estimation

In this section, we present the chosen method to determine the Etna plume transport speed by analyzing the images and then the most adapted method used to estimate the SO<sub>2</sub> emission flux with regard to our campaign configuration.

### 2.4.1. Plume Transport Speed

A key parameter to estimate the SO<sub>2</sub> emission flux is the plume transport speed. Such data has not been measured during the remote measurement campaign. Each sequence contains a few hundred images, corresponding to a few minutes of measurement. Following the method explained in Aiuppa et al. (2015) [50], it is possible to determine an average transport speed after determining its vertical and horizontal components using the reconstructed images of SO<sub>2</sub> SCD (or mass of SO<sub>2</sub> per surface unit). Two cross sections are fixed vertically, separated by a distance  $d_v$  and two horizontally separated by a distance  $d_h$ , corresponding to the number of pixels between the cross sections multiplied by the length of a pixel. By calculating the mean SO<sub>2</sub> SCD along the cross sections, we obtain two time-series, one vertically and one horizontally tracking the evolution over time of SO<sub>2</sub> SCD in the plume. The cross correlation of both time-series let us determine the time shift  $t_s$ , which represents the time necessary for the plume passing through the first vertical (or horizontal) cross section to reach the

second cross section. The appropriate time shift is the one giving the best cross-correlation coefficient between the two time-series. A representation of the cross sections is presented in Figure 4a.

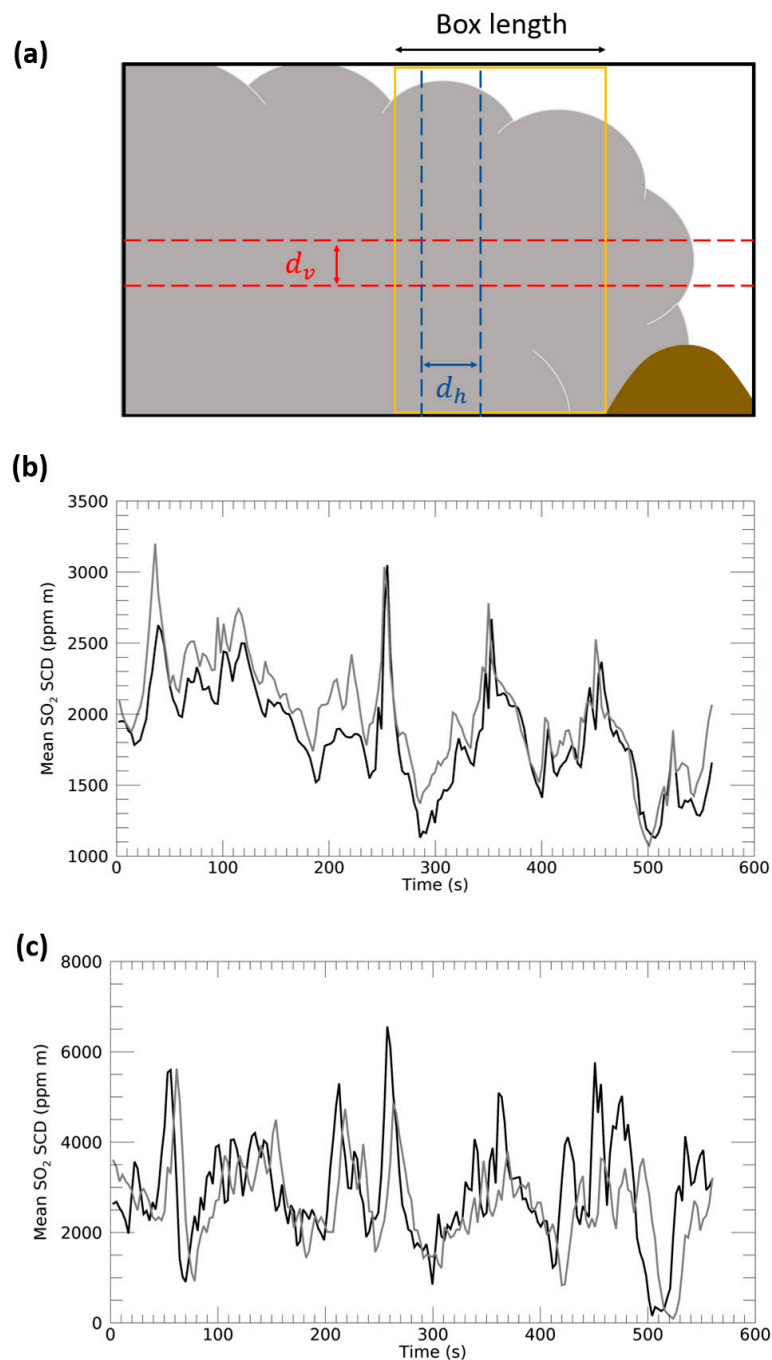


**Figure 4.** (a) A schematic representation of the scene with two vertical cross sections in blue separated by a distance  $d_h$  and two horizontal cross sections in red separated by a distance  $d_v$  to determine, respectively, the horizontal and vertical contribution of plume transport speed, and the box fixed close to the emission source for the  $\text{SO}_2$  emission flux estimation in yellow, (b) the time-series of the mean  $\text{SO}_2$  slant column densities (SCD) of the two horizontal cross sections for the first 200 images of sequence B, and (c) the time-series of the mean  $\text{SO}_2$  SCD of the two vertical cross sections for the first 200 images of sequence B.

Figure 4b,c present the  $\text{SO}_2$  mean SCD values evolutions along 200 images of sequence B, for the vertical cross sections separated by a distance  $d_v$  corresponding to 5 pixels (i.e., ~14 m) and the horizontal

cross sections separated by a distance  $d_h$  corresponding to 20 pixels (i.e., ~56 m), to characterize the plume transport speed. The plume transport speed  $v$  in  $\text{m s}^{-1}$  is then calculated by following Equation (2).

$$v = \left( \sqrt{d_h^2 + d_v^2} \right) / t_s \quad (2)$$

#### 2.4.2. Box Method for the Emission Flux Estimation

Different methods to derive the  $\text{SO}_2$  emission flux from the  $\text{SO}_2$  slant column densities (or mass of  $\text{SO}_2$ ) exist such as a traverse method, delta-M method, box method, or an inverse modelling method [51]. Most methods are adapted to satellite or airborne measurements of volcanic plumes. Instantaneous  $\text{SO}_2$  mass loading measurements from remote instruments represent the budget between emitted and lost  $\text{SO}_2$ . Therefore, when calculating gas fluxes, the  $\text{SO}_2$  loss has to be taken into account. The loss is mainly due to  $\text{SO}_2$  oxidation into sulfuric acid droplets and  $\text{SO}_2$  volume dilution, making its detection below a given threshold impossible. The rate of gas loss is related to the meteorological conditions and its inclusion may depend on the measurement settings. In our case, measurements were carried very close to the source vent by using high temporal and spatial resolutions, and located to altitudes larger than 3 km above sea level, close to the free troposphere. These conditions of acquisition allow us to neglect the  $\text{SO}_2$  loss factor [52]. One of the simplest and most adapted method to derive the first estimation of the emission flux of  $\text{SO}_2$  is the box method. It consists in defining a box, as presented with the yellow box in Figure 4a, calculating the total mass of  $\text{SO}_2$  in the box and then multiplying it by the plume age. The plume age is the time the plume needs to cross the box. It is obtained by multiplying the box length with the average plume transport speed  $v$ . In order to lower the uncertainties of the  $\text{SO}_2$  emission flux estimation, the fixed box is placed as close as possible to the emission source.

### 3. Results

#### 3.1. Training Dataset

The spectral image classification methodology was conducted using five images of the third sequence recorded on 26 June 2015. Those images have been retrieved pixel-by-pixel with the LARA model for a previous study presented in Huret et al. (2019) [34]. They are used here as a training dataset composed of 102,400 spectra. Different ranges of values assigned to the two indexes were tested to determine the best compromise between the number of classes obtained, which means the number of different patterns of spectra, and the range size limit to keep as much information as possible by classifying the images.

##### 3.1.1. Interval Width for $I_{O_3}$ Index

Four ranges of values for the integrated BT values have been tested: 10, 50, 100, and 500  $\text{K cm}^{-1}$ . The main results obtained for each tested value with a fixed value of 1 K for the range of mean BT in the spectral Band 2 is presented in Table 2. The only  $I_{O_3}$  range value showing a significant difference is 500  $\text{K cm}^{-1}$  with only ~26% of the pixels with less than 10% of relative standard deviation for plume pixels against ~48% for ranges of 10, 50, and 100  $\text{K cm}^{-1}$ .

**Table 2.** Main results for the tested ranges of values of  $I_{O_3}$  indexes.

Tested Ranges (K cm <sup>-1</sup> )	Percent of Plume Pixels/Classes with Relative Standard Deviation on SO <sub>2</sub> SCD < 10%	Number of Classes with a Relative Standard Deviation on SO <sub>2</sub> SCD < 10%
10	47.7/35.1	629
50	47.1/29.7	133
100	48/30.6	78
500	25.9/20.4	21

### 3.1.2. Interval Width for $I_{SO_2}$ Index

Three ranges of values for the mean BT have been tested: 1, 5, and 10 K. The main results obtained for each value with a fixed range value of 100 K cm<sup>-1</sup> for the integrated values in the spectral Band 1 are presented in Table 3. The tested range values for the mean BT, attributed to  $I_{SO_2}$ , only gives satisfying results for the range value of 1 K. The ranges of 5 and 10 K induce an important loss of pixels in classes with less than 10% of a relative difference in the SO<sub>2</sub> standard deviation in classes.

**Table 3.** Main results for the tested ranges for values of  $I_{SO_2}$  indexes.

Tested Ranges (K)	Percent of Plume Pixels/Classes with Relative Standard Deviation on SO <sub>2</sub> SCD < 10%	Number of Classes with Relative Standard Deviation on SO <sub>2</sub> SCD < 10%
1	48/30.6	78
5	14.1/21.7	18
10	6.3/14.5	9

The chosen spectral image classification configuration with the best compromise is a range of 100 K cm<sup>-1</sup>, between two values of integrated BT for  $I_{O_3}$ , and a range of 1 K, between two values of mean BT for  $I_{SO_2}$ .

### 3.1.3. Class Weight Distribution

Figure 5a,b represent the weight attributed to each index  $I_{O_3}$  and  $I_{SO_2}$ , respectively. The different bumps in the distributions highlight three main features from the images, which we can call clusters. The first cluster (1) corresponds to the clear sky pixels with  $I_{O_3}$  index < 25 and  $I_{SO_2}$  index < 30, which is equivalent to an integrated value of the BT below 23,500 K cm<sup>-1</sup> and a mean BT below 230 K. The second cluster (2) encompasses the plume pixels with  $I_{O_3}$  indexes in the range of 25 to 75 and  $I_{SO_2}$  indexes in the range of 30 to 90, equivalent to integrated BT values in the range of [23,500:28,500] K cm<sup>-1</sup> and mean BT in the range of [230:290] K. Then, the third cluster (3) collects the ground pixels with  $I_{O_3}$  index > 75 and  $I_{SO_2}$  index > 90, equivalent to an integrated BT greater than 28,500 K cm<sup>-1</sup> and a mean BT above 290 K. The distribution of the number of pixels for each  $I_{SO_2}$  is wider in the plume cluster than the distribution of pixels for  $I_{O_3}$ . The pixels have a thinner distribution along  $I_{SO_2}$  indexes with a total number of pixels around 3000 for the higher peaks while the higher peak of the total number of pixels along  $I_{O_3}$  reaches 4000. The diversity of  $I_{SO_2}$  values for one  $I_{O_3}$  is greater when considering the plume part of the image. This highlights the added value of the  $I_{SO_2}$  indexes to get information about SO<sub>2</sub> SCD from data using the two layers classification methodology.

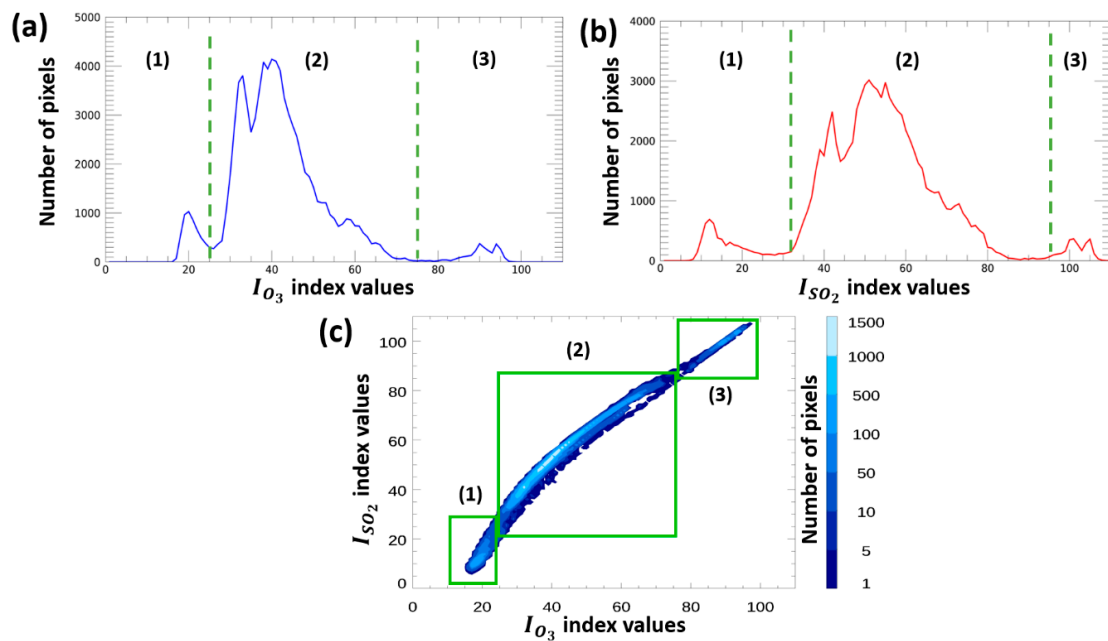


**Figure 5.** (a) Total number of pixels according to each  $I_{O_3}$  index value and (b) total number of pixels according to each  $I_{SO_2}$  index value with three parts of each distribution separated by green dashed lines. (c) 3D distribution of the number of pixels in each class with green boxes and dashed lines enlighten three clusters: (1) clear sky, (2) plume, and (3) ground.

The 2D distribution of the number of pixels in each class (see Figure 5c) has a very linear shape. However, the third dimension corresponding to the weight of each class, let us find the three main features from the images with lighter blue contours. Most of the pixels are situated in the cluster related to the plume.

As presented in Huret et al. (2019) [34], the retrieval of  $SO_2$  SCD must respect two threshold values to be considered of good quality: a normalized  $\chi^2 < 10$  and an error on the retrieved scaling factor on the  $SO_2$  SCD calculated by the LARA model that must be lower than 10%. Taking into account those threshold values, the  $SO_2$  SCD corresponding to each pair of  $(I_{O_3}, I_{SO_2})$  is calculated by taking the average value in each class of the  $SO_2$  SCD obtained with the pixel-by-pixel method for the training dataset. Around 50% of the classes corresponding to the plume part have a relative standard deviation of  $<10\%$  and  $\sim 90\%$  have a relative standard deviation of  $<15\%$ . Some classes only contain a couple of pixels from the five images. To ensure that a class corresponds to a sufficiently characteristic spectral pattern of the plume, we consider that each class must contain at least 0.01% of the total number of plume pixels from the dataset. Hence, the classes from the training dataset must contain at least seven pixels. After applying this criterion, we have 195 remaining classes corresponding to  $\sim 68,000$  pixels (99.7% of the plume pixels). In the end, 66% of the pixels from the training dataset are used to create a library to reconstruct images of  $SO_2$  SCD (ppm m) or  $SO_2$  mass per surface unit ( $g\ m^{-2}$ ) for the other sequences of Table 1. The other 34% corresponds to clear sky pixels, earth surface pixels, and plume pixels with LARA retrieval parameters above threshold values.

### 3.1.4. Analysis of the Classification Accuracy

A way to evaluate the accuracy of the classification using the five images of the training dataset is to see how correlated are the  $SO_2$  SCD values from the pixel-by-pixel retrieval and the  $SO_2$  SCD from the library created thanks to the classification, as shown in Figure 6. As presented in Huret et al. 2019 [34], the parameters used to define the Etna plume captured with Hyper-Cam (altitude, thickness, and an additional temperature with regard to ambient temperature) can have a significant impact on the  $SO_2$  SCD retrieval close to the crater. Hence, for the interpretation of the results, we applied the same

procedure and separated the five images of the training dataset in two parts, “diluted plume part” and “dense plume part”, along the same vertical line. The first order regression of the correlation points of the diluted plume part, in red, gives a slope of 0.97 following Equation (3).

$$SO_2SCD_{library} = 0.97 \times SO_2SCD_{pixel\ by\ pixel} + 88.9 \quad (3)$$

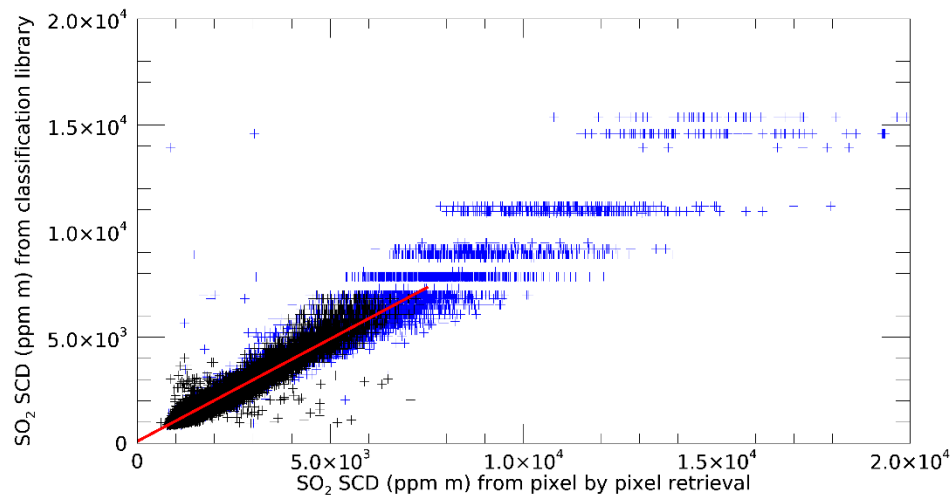


**Figure 6.** Example of correlation between the  $SO_2$  SCD of the plume pixels of the training dataset of 26 June 2015 from the pixel-by-pixel method with the reconstructed values using the classification library. The black points are from the “diluted part of the plume” and the blue point are from the “dense part of the plume”. The first order regression of the “diluted part of the plume” is in red with a slope of 0.97 and a determination coefficient of 0.94.

The correlation of the diluted plume part points is compact. When  $SO_2$  SCD values exceed 7000 ppm m, we observe a wider range of  $SO_2$  SCD values from the pixel-by-pixel retrieval attributed to one class. The correlation points over 7000 ppm m extending over a wider range of values represent only 2.7% of the plume pixels of the training dataset.

The results obtained with the training dataset composed of five images are, thus, very satisfying. The library created with the 195 plume classes was applied to retrieve the images of the other sequences.

### 3.2. Tested Dataset

We apply the method to the 900 images of the three sequences previously presented in Table 1. Those sequences have been captured with similar instrument orientation as the plume of Mount Etna was transported in the same direction over the days of the campaign. Each image has ground pixels situated at the bottom right part of the images, clear sky pixels at the upper right part of the images, and the rest being plume pixels. All the sequences are classified independently, and each pixel is labeled with its corresponding  $I_{O_3}$  and  $I_{SO_2}$  indexes. As mentioned in Section 2.2, the classes with less than 0.01% of the total number of plume pixels from the sequences are excluded. Moreover, since our interest is in plume pixels, we only consider classes corresponding to  $I_{O_3}$  indexes with BT integral values in the range of [23,500:28,500]  $K\ cm^{-1}$ .

Table 4 sums up the characteristics of the classification of the three tested datasets such as the time to classify an image, the proportion of patterns necessary to reconstruct the  $SO_2$  SCD images, and those who are not listed in the library. The time necessary to classify a sequence depends on three elements: the size of the image (i.e., number of pixels), the number of images in the dataset, and the spectral resolution. The retrieval is in the order of ~15 s for an image with a spectral resolution of  $4\ cm^{-1}$  and in the order of ~35 s for an image with a spectral resolution of  $2\ cm^{-1}$ . In comparison with the pixel-by-pixel method, which demands a week of calculation for an image of sequence

B, the classification and retrieval using the library only takes ~34 s to retrieve an image from that same sequence.

**Table 4.** Main characteristics of the classification of the tested sequences.

Sequence #	Classification Time (s/Image)	Number of Classes: In the Plume/Out of Plume Library	Percent of Pixels from Plume Out of the Library
A	36.7	560/109	22.5
B	33.8	687/156	20.6
C	15.3	754/99	15.0

Even though Mount Etna was in a quiescent stage of activity (i.e., not in eruption) and the plume was transported in the same direction, the training dataset represents only a part of the variety of the SO<sub>2</sub> spectral patterns of the Etna NEC plume. The library created allows the massive retrieval of three sequences with only 15% to ~22% of unlisted plume pixels patterns, distributed in the whole sequence. One image example from each of the three datasets is presented in Figure 7 with the missing pixels colored in blue. As can be seen in Figure 7a, the sequence A has higher values of mass of SO<sub>2</sub> per surface unit in the range of ~2.5–35 g m<sup>-2</sup> in comparison with sequence B and C with values ranging from ~1–20 g m<sup>-2</sup>. The example images from sequences A and B suggest that most of the missing pixels are close to the emission source. Nevertheless, the unlisted pixels of each sequence are not only limited to the denser part of the plume. If we look at those pixels in more detail, 70% of the missing pixels of sequence A, 92% from the one of sequence B, and 29% from the unlisted ones of sequence C, are in the denser part of the plume (i.e.,  $I_{O_3}$  indexes > 50).

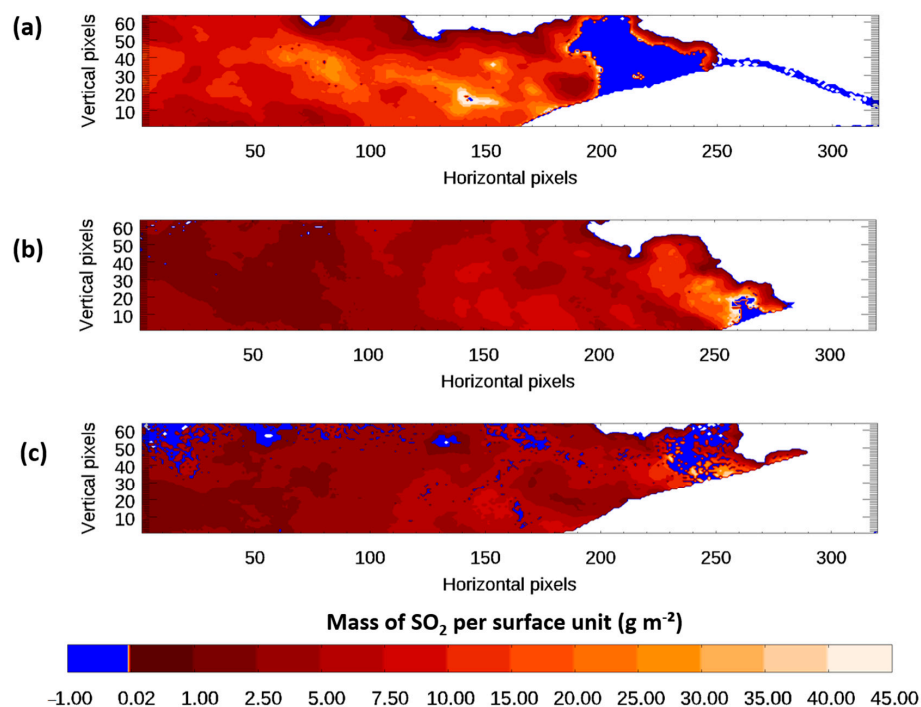


**Figure 7.** Examples of mass of SO<sub>2</sub> per surface unit (g m<sup>-2</sup>) images retrieved with the training dataset library with the unlisted class pixels colored in blue: (a) Sequence A (23 June 2015—08:13:33 UTC), (b) Sequence B (26 June 2015—08:25:33 UTC), and (c) Sequence C (26 June 2015—07:18:08 UTC).



### 3.3. SO<sub>2</sub> Emission Flux

The three tested datasets have more than 80% of their plume pixels included in the library, which is enough to estimate the SO<sub>2</sub> emission flux.

Over the few minutes of measurement, the vertical contribution of the plume transport speed was null or negligible with cross correlation coefficients of determination from 0.83 to 0.89. The vertical cross correlations indicate that the Etna plume propagated horizontally with a plume transport speed going from  $\sim 5.8$  m s<sup>-1</sup> (sequence A) to  $\sim 6.6$  m s<sup>-1</sup> (sequences B and C). Mount Etna was in a passive degassing period and the sequences recorded lasted a few minutes. Based on the cross-correlation calculation results, the plume transport speed remained uniform and was considered constant.

The boxes are fixed with a horizontal length corresponding to 50 pixels ( $\sim 140$  m) and a vertical length corresponding to the 64 vertical pixels ( $\sim 179$  m) of each of the three sequences and are placed close to the ground part of the image. The time evolution of the SO<sub>2</sub> emission flux of the three sequences is presented in Figure 8 and the average results from the three datasets are presented in Table 5. The position and the small size of the boxes,  $\sim 25.2$  km<sup>2</sup>, allow us to capture the heterogeneity of the concentration of SO<sub>2</sub> coming out of the crater. The variability of the SO<sub>2</sub> emission flux is important, with values going from single to double within seconds, especially for the sequences A and B. Short videos showing the dynamism of the plume for the three sequences are available in the additional material of this paper (externally hosted Supplementary Materials Files 1–3).

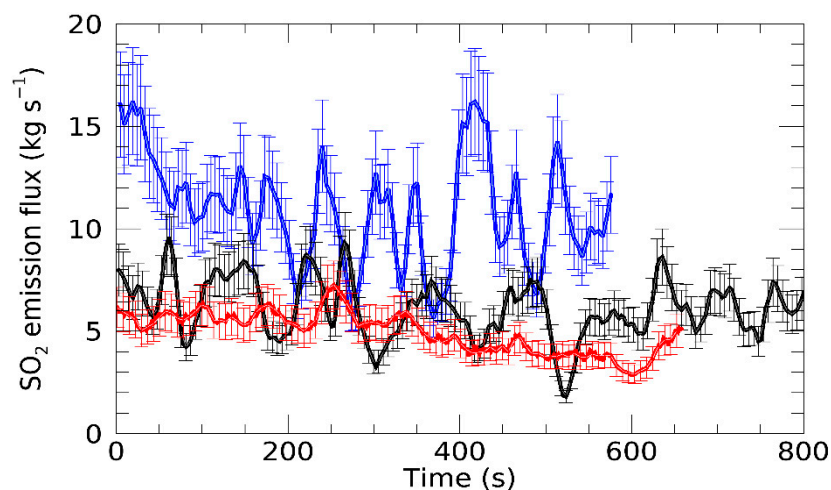


**Figure 8.** Time evolution of the SO<sub>2</sub> emission flux estimation of the three sequence (A in blue, B in black, and C in red) and corresponding error-bars.

**Table 5.** Average plume transport speed, average mass of SO<sub>2</sub> per surface unit, and average SO<sub>2</sub> emission flux over the sequences with a corresponding standard deviation ( $1\sigma$ ).

#	Plume Transport Speed	Average Mass of SO <sub>2</sub> Per Surface Unit	Average SO <sub>2</sub> Emission Flux	
	(m s <sup>-1</sup> )	(g m <sup>-2</sup> )	(kg s <sup>-1</sup> )	(t day <sup>-1</sup> )
A	5.83	10.54 ± 7.76	10.87 ± 2.61	938.84 ± 225.25
B	6.66	5.34 ± 4.53	6.13 ± 1.41	529.79 ± 122.13
C	6.62	4.56 ± 2.93	4.95 ± 0.98	427.51 ± 85.15

## 4. Discussion

The number of patterns of the training dataset is small in comparison to the diversity of Mount Etna behaviors [2]. Nevertheless, we managed to retrieve the SO<sub>2</sub> SCD of three sequences from the IMAGETNA campaign.

The estimation of the NEC SO<sub>2</sub> emission flux shows how variable the emissions are in the scale of a few seconds. Most of the SO<sub>2</sub> emission fluxes from Mount Etna in the literature are values averaged over hours or days. Aiuppa et al. (2008) [53] estimated the flux of SO<sub>2</sub> from the NEC to be around 352 t day<sup>-1</sup> with an error around 20% during a passive degassing state of Mount Etna in July 2007 using routine DOAS traverse measurements. La Spina et al. 2010 [54] obtained SO<sub>2</sub> flux from 270 to 1000 t day<sup>-1</sup> with a standard error of 30% using a ground-based lightweight open-path Fourier transform infrared spectrometry in active mode with a portable infrared lamp. Gliß et al. (2018) [55] presented an average estimation, from 15 min of ground-based UV camera measurements on 16 September 2015, of the NEC SO<sub>2</sub> emission flux of ~8 kg s<sup>-1</sup> (equivalent to ~690 t day<sup>-1</sup>). In Prata and Bernardo (2014), the obtained SO<sub>2</sub> emission flux is in the range of 10–20 kg s<sup>-1</sup> (equivalent to ~860–1730 t day<sup>-1</sup>) along a period of 7 h of measurement in September 2003 with data acquired every 4–6 min using the multifilter thermal infrared camera system Cyclops [27]. Our results are in the range of values obtained in the literature. Nevertheless, our estimation of the North East Crater SO<sub>2</sub> emission flux are only partial estimations since the plume of Mount Etna was trimmed by the field of view of the Hyper-Cam imager, capturing only a part of the total plume of the NEC, which, moreover, would be the gas emission of only one of the four main craters of Mount Etna.

Oppenheimer et al. (2006) presented SO<sub>2</sub> column amounts from ground-based UV spectrometer measurements with a scattered skylight as a UV source, ranging from 0.5 to 3 g m<sup>-2</sup> for measurements within La Voragine summit crater, which was the strongest gas sources at the moment of the measurements, and values up to 2 g m<sup>-2</sup> for measurements of the plume of Etna from a location at ~2 km from the craters [56]. The SO<sub>2</sub> emission flux also measured by UV spectroscopy on that day was ~11 kg s<sup>-1</sup> (equivalent to ~950 t day<sup>-1</sup>). The SO<sub>2</sub> column amount from our three datasets are a bit higher with average values ranging from 4.5 to 10.5 g m<sup>-2</sup>.

One of the main sources of uncertainties is related to the estimation of the plume transport speed. The error on the retrieval of SO<sub>2</sub> SCD also impact the estimation of the SO<sub>2</sub> emission flux. For the training dataset, the average error is ~5.8%. The uncertainties of the SO<sub>2</sub> emission flux estimation are mostly related to the plume transport speed determination and the averaging of the SO<sub>2</sub> slant column densities calculated in each class outcoming from the training dataset classification. The error on the plume transport speed is directly linked to the estimation error on the distance from the instrument to the plume that was determined visually with the relief. We consider this error as being ~10%, so that the average error on the estimate of the SO<sub>2</sub> emission flux is ~16% for the presented datasets. It is in the range or even lower than the uncertainties on SO<sub>2</sub> emission flux of similar studies like the one from Gabrieli et al. on Kilauea volcano in Hawaii with less than 25% of error mainly induced by the determination of wind velocities [57].

## 5. Conclusions

In this paper, we have presented a spectral classification methodology of the Hyper-Cam images pixels from the IMAGETNA campaign. The network architecture is composed of two layers corresponding to two features extracted from the spectral bands of O<sub>3</sub> and SO<sub>2</sub>. One feature characterizing the opacity of the plume and the second one characterizing the concentration in SO<sub>2</sub>. The accuracy of the classification results was evaluated in correlation with the results of the time-consuming pixel-by-pixel retrieval, giving a first order regression slope of 0.97 and a very good determination coefficient of 0.94 in the diluted part of the training dataset. This method allows a fast and accurate reconstruction of SO<sub>2</sub> slant column density images of three sequences from the IMAGETNA campaign. Each image is processed in less than 40 s instead of 7 days with a pixel-by-pixel retrieval methodology.

The plume transport speed was determined by calculating the cross correlation between time series of mean SO<sub>2</sub> slant column densities along two horizontal and two vertical cross sections. The SO<sub>2</sub> emission flux relative of the North East Crater from Mount Etna was estimated using the “box method” and the results ranged from ~5 to 11 kg s<sup>-1</sup> (~430–940 t day<sup>-1</sup>) with an error of ~16%.

A way to improve the developed methodology would be to include neighborhood pixels information. The results presented here were performed on sequences of a few minutes with similar weather conditions, plume level of activity, and measurement characteristics. In the future, it would be interesting to test this image pixels classification method on datasets with other characteristics to enrich the training dataset and develop a fast procedure to enlarge the library, and, thus, retrieve the missing features. A wider field of view or a different geometrical configuration of measurement, making it possible to capture the entire Etna plume, would also allow comparisons to be made with other methods of spectra retrieval and estimation of the SO<sub>2</sub> emission flux.

The use of a hyperspectral infrared imager, with an acquisition time of images of a few s, associated with the classification and retrieval time of the spectra of an image lower than a min, would allow the monitoring of the evolution of SO<sub>2</sub> emission flux in near-real-time at a high frequency. All of this would contribute to help prevent any hazards coming from active volcanoes but also strengthen the attractiveness and interest of this technology for volcanic gas emissions monitoring.

**Supplementary Materials:** The following are available online at <http://www.mdpi.com/2072-4292/12/24/4107/s1>, Externally hosted Supplementary File 1: SO<sub>2</sub> Slant column densities from sequence A Link: <https://hal.uca.fr/hal-02988223>. Externally hosted Supplementary File 2: SO<sub>2</sub> Slant column densities from sequence B Link: <https://hal.uca.fr/hal-02988226>. Externally hosted Supplementary File 3: SO<sub>2</sub> Slant column densities from sequence C. Link: <https://hal.uca.fr/hal-02988229>.

**Author Contributions:** Conceptualization, C.S., N.H., and S.P. Methodology, C.S., N.H., and S.P. Software, C.S. and S.P. Validation, C.S. Formal analysis, C.S., N.H., and S.P. Investigation, C.S. Resources, N.H., S.P., M.G., and V.C. Data curation, C.S. and S.P. Writing—original draft preparation, C.S. Writing—review & editing, N.H., S.P., M.G., and V.C. Visualization, C.S. Supervision, C.S. Funding acquisition, N.H. and V.C. All authors have read and agreed to the published version of the manuscript.

**Funding:** This project IMAGETNA is funded by the LABEX Voltaire n° ANR-10-LABX-100-01 from the ANR agency and the French national program of chemistry LEFE-CHAT from CNRS-INSU. This research was funded through HEMERA infrastructure (via the European Union's Horizon 2020 research and Innovation program (grant N°730970)), by Centre National d'Etudes Spatiales and Institut National des Sciences de L'Univers (CNES/INSU APR 2020).

**Acknowledgments:** We sincerely thank the INGV for providing logistic at Etna and get very good conditions for the campaign. We thank A. Huot (TELOPS Inc.) for fruitful exchanges and her availability during the campaign. We thank the AERIS Data and Service for the Atmosphere infrastructure ([www.aeris-data.fr/](http://www.aeris-data.fr/)), which provides us the computer capacity for data processing. This work is a part of C.S. PhD thesis supported by the Doctoral School of Fundamental Sciences of the Université Clermont Auvergne.

**Conflicts of Interest:** The authors declare no conflict of interest.

## References

1. Doocy, S.; Daniels, A.; Dooling, S.; Gorokhovich, Y. The human impact of volcanoes: A historical review of events 1900-2009 and systematic literature review. *PLoS Curr.* **2013**, *5*. [[CrossRef](#)] [[PubMed](#)]
2. Allard, P.; Behncke, B.; D'Amico, S.; Neri, M.; Gambino, S. Mount Etna 1993–2005: Anatomy of an evolving eruptive cycle. *Earth-Sci. Rev.* **2006**, *78*, 85–114. [[CrossRef](#)]
3. Caltabiano, T.; Romano, R.; Budetta, G. SO<sub>2</sub> flux measurements at Mount Etna (Sicily). *J. Geophys. Res.* **1994**, *99*, 12809–12819. [[CrossRef](#)]
4. Oppenheimer, C. Volcanic Degassing. In *Treatise on Geochemistry*; Holland, H.D., Turekian, K.K., Eds.; Elsevier Inc.: Amsterdam, The Netherlands, 2003; pp. 123–166. [[CrossRef](#)]
5. Aiuppa, A.; Moretti, R.; Federico, C.; Giudice, G.; Gurrieri, S.; Liuzzo, M.; Papale, P.; Shinohara, H.; Valenza, M. Forecasting Etna eruptions by real-time observation of volcanic gas composition. *Geology* **2007**, *35*, 1115–1118. [[CrossRef](#)]
6. Sparks, R.S.J. Forecasting volcanic eruptions. *Earth Planet. Sci. Lett.* **2003**, *210*, 1–15. [[CrossRef](#)]
7. D'Aleo, R.; Bitetto, M.; Delle Donne, D.; Coltelli, M.; Coppola, D.; McCormick Kilbride, B.; Pecora, E.; Ripepe, M.; Salem, L.C.; Tamburello, G.; et al. Understanding the SO<sub>2</sub> degassing budget of Mt Etna's paroxysms: First clues from the December 2015 sequence. *Front. Earth Sci.* **2019**, *6*. [[CrossRef](#)]

8. Delle Donne, D.; Aiuppa, A.; Bitetto, M.; D'Aleo, R.; Coltelli, M.; Coppola, D.; Pecora, E.; Ripepe, M.; Tamburello, G. Changes in SO<sub>2</sub> flux regime at Mt. Etna captured by automatically processed ultraviolet camera data. *Remote Sens.* **2019**, *11*, 1201. [[CrossRef](#)]
9. Burton, M.; Allard, P.; Muré, F.; La Spina, A. Magmatic gas composition reveals the source depth of slug-driven strombolian explosive activity. *Science* **2007**, *317*, 227–230. [[CrossRef](#)]
10. Vergnolle, S.; Jaupart, C. Dynamics of degassing at Kilauea Volcano, Hawaii. *J. Geophys. Res.* **1990**, *95*, 2793–2809. [[CrossRef](#)]
11. Robock, A. Volcanic eruptions and climate. *Rev. Geophys.* **2000**, *38*, 191–219. [[CrossRef](#)]
12. Hansell, A.; Oppenheimer, C. Health Hazards from Volcanic Gases: A Systematic Literature Review. *Arch. Environ. Health Int. J.* **2004**, *59*, 628–639. [[CrossRef](#)] [[PubMed](#)]
13. Williams-Jones, G.; Rymer, H. Hazards of Volcanic Gases. In *The Encyclopedia of Volcanoes*, 2nd ed.; Sigurdsson, H., Houghton, B., Rymer, H., Stix, J., McNutt, S., Eds.; Elsevier Inc.: Amsterdam, The Netherlands, 2015; pp. 985–992. [[CrossRef](#)]
14. Prata, F.; Bluth, G.; Werner, C.; Realmunto, V.; Carn, S.; Watson, M. Remote sensing of gas emissions from volcanoes. In *Monitoring Volcanoes in the North Pacific: Observations from Space*; Dean, K.G., Dehn, J., Eds.; Springer: Berlin/Heidelberg, Germany, 2015; pp. 145–186. [[CrossRef](#)]
15. Allard, P. Endogenous magma degassing and storage at Mount Etna. *Geophys. Res. Lett.* **1997**, *24*, 2219–2222. [[CrossRef](#)]
16. Carn, S.A.; Krueger, A.J.; Arellano, S.; Krotkov, N.A.; Yang, K. Daily monitoring of Ecuadorian volcanic degassing from space. *J. Volcanol. Geotherm. Res.* **2008**, *176*, 141–150. [[CrossRef](#)]
17. Carn, S.A.; Clarisse, L.; Prata, A.J. Multi-decadal satellite measurements of global volcanic degassing. *J. Volcanol. Geotherm. Res.* **2016**, *311*, 99–134. [[CrossRef](#)]
18. Gouhier, M.; Paris, R. SO<sub>2</sub> and tephra emissions during the December 22, 2018 Anak Krakatau eruption. *Volcanica* **2019**, *2*, 91–103. [[CrossRef](#)]
19. Theys, N.; Hedelt, P.; De Smedt, I.; Lerot, C.; Yu, H.; Vlietinck, J.; Pedernana, M.; Arellano, S.; Galle, B.; Fernandez, D.; et al. Global monitoring of volcanic SO<sub>2</sub> degassing with unprecedented resolution from TROPOMI onboard Sentinel-5 Precursor. *Sci. Rep.* **2019**, *9*, 2643. [[CrossRef](#)]
20. Watson, I.M.; Realmunto, V.J.; Rose, W.I.; Prata, A.J.; Bluth, G.J.S.; Gu, Y.; Bader, C.E.; Yu, T. Thermal infrared remote sensing of volcanic emissions using the moderate resolution imaging spectroradiometer. *J. Volcanol. Geotherm. Res.* **2004**, *135*, 75–89. [[CrossRef](#)]
21. Prata, A.J.; Kerkmann, J. Simultaneous retrieval of volcanic ash and SO<sub>2</sub> using MSG-SEVIRI measurements. *Geophys. Res. Lett.* **2007**, *35*, L05813:1–L05813:6. [[CrossRef](#)]
22. Karagulian, F.; Clarisse, L.; Clerbaux, C.; Prata, A.J.; Hurtmans, D.; Coheur, P.F. Detection of volcanic SO<sub>2</sub>, ash, and H<sub>2</sub>SO<sub>4</sub> using the Infrared Atmospheric Sounding Interferometer (IASI). *J. Geophys. Res. Atmos.* **2010**, *115*, D00L02:1–D00L02:10. [[CrossRef](#)]
23. Carn, S.A.; Strow, L.L.; de Souza-Machado, S.; Edmonds, Y.; Hannon, S. Quantifying tropospheric volcanic emissions with AIRS: The 2002 eruption of Mt. Etna (Italy). *Geophys. Res. Lett.* **2005**, *32*, L02301:1–L02301:5. [[CrossRef](#)]
24. Mori, T.; Burton, M. The SO<sub>2</sub> camera: A simple, fast and cheap method for ground-based imaging of SO<sub>2</sub> in volcanic plumes. *Geophys. Res. Lett.* **2006**, *33*, L24804:1–L24804:5. [[CrossRef](#)]
25. Galle, B.; Oppenheimer, C.; Geyer, A.; McGonigle, A.J.S.; Edmonds, M.; Horrocks, L. A miniaturised ultraviolet spectrometer for remote sensing of SO<sub>2</sub> fluxes: A new tool for volcano surveillance. *J. Volcanol. Geotherm. Res.* **2003**, *119*, 241–254. [[CrossRef](#)]
26. Edmonds, M.; Herd, R.A.; Galle, B.; Oppenheimer, C.M. Automated, high time-resolution measurements of SO<sub>2</sub> flux at Soufrière Hills Volcano, Montserrat. *Bull. Volcanol.* **2003**, *65*, 578–586. [[CrossRef](#)]
27. Prata, A.J.; Bernardo, C. Retrieval of sulfur dioxide from a ground-based thermal infrared imaging camera. *Atmos. Meas. Tech.* **2014**, *7*, 2807–2828. [[CrossRef](#)]
28. Merucci, L.; Burton, M.; Corradini, S.; Salerno, G.G. Reconstruction of SO<sub>2</sub> flux emission chronology from space-based measurements. *J. Volcanol. Geotherm. Res.* **2011**, *206*, 80–87. [[CrossRef](#)]
29. Galle, B.; Johansson, M.; Rivera, C.; Zhang, Y.; Kihlman, M.; Kern, C.; Lehmann, T.; Platt, U.; Arellano, S.; Hidalgo, S. Network for Observation of Volcanic and Atmospheric Change (NOVAC)—A global network for volcanic gas monitoring: Network layout and instrument description. *J. Geophys. Res. Atmos.* **2010**, *115*, D05304:1–D05304:19. [[CrossRef](#)]

30. Salerno, G.G.; Burton, M.R.; Oppenheimer, C.; Caltabiano, T.; Randazzo, D.; Bruno, N.; Longo, V. Three-years of SO<sub>2</sub> flux measurements of Mt. Etna using an automated UV scanner array: Comparison with conventional traverses and uncertainties in flux retrieval. *J. Volcanol. Geotherm. Res.* **2009**, *183*, 76–83. [[CrossRef](#)]
31. Queißer, M.; Burton, M.; Theys, N.; Pardini, F.; Salerno, G.; Caltabiano, T.; Varnam, M.; Esse, B.; Kazahaya, R. TROPOMI enables high resolution SO<sub>2</sub> flux observations from Mt. Etna, Italy, and beyond. *Sci. Rep.* **2019**, *9*, 957. [[CrossRef](#)]
32. D’Aleo, R.; Bitetto, M.; Donne, D.D.; Tamburello, G.; Battaglia, A.; Coltelli, M.; Patanè, D.; Prestifilippo, M.; Sciotto, M.; Aiuppa, A. Spatially resolved SO<sub>2</sub> flux emissions from Mt Etna. *Geophys. Res. Lett.* **2016**, *43*, 7511–7519. [[CrossRef](#)]
33. Smekens, J.F.; Gouhier, M. Observation of SO<sub>2</sub> degassing at Stromboli volcano using a hyperspectral thermal infrared imager. *J. Volcanol. Geotherm. Res.* **2018**. [[CrossRef](#)]
34. Huret, N.; Segonne, C.; Payan, S.; Salerno, G.; Catoire, V.; Ferrec, Y.; Roberts, T.; Pola Fossi, A.; Rodriguez, D.; Croizé, L.; et al. Infrared Hyperspectral and Ultraviolet Remote Measurements of Volcanic Gas Plume at MT Etna during IMAGETNA Campaign. *Remote Sens.* **2019**, *11*, 1175. [[CrossRef](#)]
35. Wright, R.; Lucey, P.; Crites, S.; Horton, K.; Wood, M.; Garbeil, H. BBM/EM design of the thermal hyperspectral imager: An instrument for remote sensing of earth’s surface, atmosphere and ocean, from a microsatellite platform. *Acta Astronaut.* **2013**, *87*, 182–192. [[CrossRef](#)]
36. Clark, M.L.; Roberts, D.A.; Clark, D.B. Hyperspectral discrimination of tropical rain forest tree species at leaf to crown scales. *Remote Sens. Environ.* **2005**, *96*, 375–398. [[CrossRef](#)]
37. Briottet, X.; Boucher, Y.; Dimmeler, A.; Malaplate, A.; Cini, A.; Diani, M.; Bekman, H.; Schwering, P.; Skauli, T.; Kasen, I.; et al. Military applications of hyperspectral imagery. In Proceedings of the Targets and Backgrounds XII: Characterization and Representation; International Society for Optics and Photonics, Defense and Security Symposium, Orlando, FL, USA, 17–21 April 2006; Volume 6239, p. 62390B.
38. Paoletti, M.E.; Haut, J.M.; Plaza, J.; Plaza, A. Deep learning classifiers for hyperspectral imaging: A review. *ISPRS J. Photogramm. Remote Sens.* **2019**, *158*, 279–317. [[CrossRef](#)]
39. Lu, D.; Weng, Q. A survey of image classification methods and techniques for improving classification performance. *Int. J. Remote Sens.* **2007**, *28*, 823–870. [[CrossRef](#)]
40. Van Damme, M.; Whitburn, S.; Clarisse, L.; Clerbaux, C.; Hurtmans, D.; Coheur, P.-F. Version 2 of the IASI NH<sub>3</sub> neural network retrieval algorithm: Near-real-time and reanalysed datasets. *Atmos. Meas. Tech.* **2017**, *10*, 4905–4914. [[CrossRef](#)]
41. Lagueux, P.; Farley, V.; Chamberland, M.; Villemaire, A.; Turcotte, C.; Puckrin, E. Design and Performance of the Hyper-Cam, an Infrared Hyperspectral Imaging Sensor. Available online: <https://www.semanticscholar.org/paper/Design-and-Performance-of-the-Hyper-Cam%2C-an-Imaging-Lagueux-Farley/2f7590496d218177bd059fe6bbab98ad69afc36e> (accessed on 14 December 2020).
42. Calvari, S.; Coltelli, M.; Müller, W.; Pompilio, M.; Scribano, V. Eruptive history of South-Eastern crater of Mount Etna, from 1971 to 1994. *Acta Vulcanol.* **1994**, *5*, 11–14.
43. Rodgers, C.D. *Inverse Methods for Atmospheric Sounding: Theory and Practice*; Atmospheric, Oceanic and Planetary Physics—Volume 2; World Scientific: Singapore, 2000.
44. Payan, S.; Camy-Peyret, C.; Jeseck, P.; Hawat, T.; Durry, G.; Lefèvre, F. First direct simultaneous HCl and ClONO<sub>2</sub> profile measurements in the Arctic Vortex. *Geophys. Res. Lett.* **1998**, *25*, 2663–2666. [[CrossRef](#)]
45. Payan, S.; Camy-Peyret, C.; Bureau, J. Comparison of Retrieved L2 Products from Four Successive Versions of L1B Spectra in the Thermal Infrared Band of TANSO-FTS over the Arctic Ocean. *Remote Sens.* **2017**, *9*, 1167. [[CrossRef](#)]
46. Butz, A.; Bösch, H.; Camy-Peyret, C.; Dorf, M.; Engel, A.; Payan, S.; Pfeilsticker, K. Observational constraints on the kinetics of the ClO-BrO and ClO-ClO ozone loss cycles in the Arctic winter stratosphere. *Geophys. Res. Lett.* **2007**, *34*, L05801:1–L05801:5. [[CrossRef](#)]
47. Payan, S.; Camy-Peyret, C.; Oelhaf, H.; Wetzell, G.; Maucher, G.; Keim, C.; Pirre, M.; Huret, N.; Engel, A.; Volk, M.C.; et al. Validation of version-4.61 methane and nitrous oxide observed by MIPAS. *Atmos. Chem. Phys.* **2009**, *9*, 413–442. [[CrossRef](#)]
48. Keim, C.; Eremenko, M.; Orphal, J.; Dufour, G.; Flaud, J.-M.; Höpfner, M.; Boynard, A.; Clerbaux, C.; Payan, S.; Coheur, P.-F.; et al. Tropospheric ozone from IASI: Comparison of different inversion algorithms and validation with ozone sondes in the northern middle latitudes. *Atmos. Chem. Phys.* **2009**, *9*, 9329–9347. [[CrossRef](#)]

49. Clough, S.A.; Shephard, M.W.; Mlawer, E.J.; Delamere, J.S.; Iacono, M.J.; Cady-Pereira, K.; Boukabara, S.; Brown, P.D. Atmospheric radiative transfer modeling: A summary of the AER codes. *J. Quant. Spectrosc. Radiat. Transf.* **2005**, *91*, 233–244. [[CrossRef](#)]
50. Aiuppa, A.; Fiorani, L.; Santoro, S.; Parracino, S.; Nuvoli, M.; Chiodini, G.; Minopoli, C.; Tamburello, G. New ground-based lidar enables volcanic CO<sub>2</sub> flux measurements. *Sci. Rep.* **2015**, *5*, 13614. [[CrossRef](#)] [[PubMed](#)]
51. Theys, N.; Campion, R.; Clarisse, L.; Brenot, H.; van Gent, J.; Dils, B.; Corradini, S.; Merucci, L.; Coheur, P.-F.; Van Roozendaal, M.; et al. Volcanic SO<sub>2</sub> fluxes derived from satellite data: A survey using OMI, GOME-2, IASI and MODIS. *Atmos. Chem. Phys.* **2013**, *13*, 5945–5968. [[CrossRef](#)]
52. McGonigle, A.J.S.; Delmelle, P.; Oppenheimer, C.; Tsanev, V.I.; Delfosse, T.; Williams-Jones, G.; Horton, K.; Mather, T.A. SO<sub>2</sub> depletion in tropospheric volcanic plumes. *Geophys. Res. Lett.* **2004**, *31*, L13201:1–L13201:4. [[CrossRef](#)]
53. Aiuppa, A.; Giudice, G.; Gurrieri, S.; Liuzzo, M.; Burton, M.; Caltabiano, T.; McGonigle, A.J.S.; Salerno, G.; Shinohara, H.; Valenza, M. Total volatile flux from Mount Etna. *Geophys. Res. Lett.* **2008**, *35*, L24302:1–L24302:5. [[CrossRef](#)]
54. La Spina, A.; Burton, M.; Salerno, G.G. Unravelling the processes controlling gas emissions from the central and northeast craters of Mt. Etna. *J. Volcanol. Geotherm. Res.* **2010**, *198*, 368–376. [[CrossRef](#)]
55. Gliß, J.; Stebel, K.; Kylling, A.; Sudbø, A. Improved optical flow velocity analysis in SO<sub>2</sub> camera images of volcanic plumes—Implications for emission-rate retrievals investigated at Mt Etna, Italy and Guallatiri, Chile. *Atmos. Meas. Tech.* **2018**, *11*, 781–801. [[CrossRef](#)]
56. Oppenheimer, C.; Tsanev, V.I.; Braban, C.F.; Cox, R.A.; Adams, J.W.; Aiuppa, A.; Bobrowski, N.; Delmelle, P.; Barclay, J.; McGonigle, A.J.S. BrO formation in volcanic plumes. *Geochim. Cosmochim. Acta* **2006**, *70*, 2935–2941. [[CrossRef](#)]
57. Gabrieli, A.; Wright, R.; Porter, J.N.; Lucey, P.G.; Honnibal, C. Applications of quantitative thermal infrared hyperspectral imaging (8–14 μm): Measuring volcanic SO<sub>2</sub> mass flux and determining plume transport velocity using a single sensor. *Bull. Volcanol.* **2019**, *81*. [[CrossRef](#)]

**Publisher’s Note:** MDPI stays neutral with regard to jurisdictional claims in published maps and institutional affiliations.



© 2020 by the authors. Licensee MDPI, Basel, Switzerland. This article is an open access article distributed under the terms and conditions of the Creative Commons Attribution (CC BY) license (<http://creativecommons.org/licenses/by/4.0/>).